A Decoupled Droop Control Strategy for Cascaded Multicell Inverter with Low-Frequency Modulation

Shuo Zhang
Department of Electrical and Computer Engineering
University of Nebraska-Lincoln
Lincoln, NE 68588-0511 USA
szhang34@huskers.unl.edu

Wei Qiao
Department of Electrical and Computer Engineering
University of Nebraska-Lincoln
Lincoln, NE 68588-0511 USA
wqiao3@unl.edu

Liyan Qu
Department of Electrical and Computer Engineering
University of Nebraska-Lincoln
Lincoln, NE 68588-0511 USA
lqu2@unl.edu

Abstract—Cascaded multicell inverter (CMI), featured by its merits of modularity and fault-tolerance, is suitable for medium-voltage applications without using bulky step-up transformers. However, little research has reported grid-forming control of the CMI for the application in the power grid with high penetrations of inverter-interfaced generation. To bridge this research gap, this paper proposes a novel droop control strategy for the CMI with a low-frequency modulation to offer inertia and reactive power support to the power grid. A decoupled Q/V droop control strategy is proposed to eliminate the coupling effect from the P/ω control loop caused by the phase-angle difference between the voltages of the CMI and the grid. The output of the Q/V control loop is set as the reference voltage for each cell of the CMI, which makes the CMI naturally a voltage source to provide a grid-forming capability. Finally, the proposed control strategy shows great active and reactive power regulation and sharing capability, which is validated by simulation on two 100 kW, 2.4 kV CMIs connected in parallel to a power grid.

Keywords—cascaded multicell inverter (CMI); decoupled droop control, low-frequency modulation (LFM).

I. INTRODUCTION

Multilevel inverter (MLI) has been considered as a promising technology for integrating large-scale renewable energy generation in the medium-voltage (MV) power grid. Among the basic MLI topologies, cascaded multicell inverter (CMI) with separate dc sources and inverters is featured by its merits of modularity, fault-tolerant ability, and simplicity of control [1]-[3]. Each cell of CMI consists of an isolated dc source and an inverter which is connected in series with that of other cells. The switches in each individual cell can work either with a high-frequency pulse-width modulation (PWM) or a low-frequency modulation (LFM) method [2]. Compared with the CMI using a high-frequency PWM, the CMI using an LFM requires a few more series-connected cells (about 10 cells) to output a near sinusoidal voltage waveform to meet the total harmonic distortion (THD) requirement. However, the LFM leads to a higher-efficiency CMI and easier thermal management for the power electronic switches and removes the need for bulky filters [4]. Moreover, by using an appropriate selected harmonic elimination (SHE) approach [4], [5], the harmonics injected into the power grid could be mitigated. On the other hand, the use of more cells could enhance the fault-tolerant ability of the CMI because it allows failure of one or more cells while satisfying the output voltage magnitude and THD requirements. These advantages make the CMI with an LFM a promising technology for MV applications.

With the increasing proportion of the inverter-interfaced renewable generation to gradually replace the fossil fuel-based generation in the power grid, the concept of grid-forming converters (GFCs) has been introduced to tackle the low-inertia issue and the frequency stability issue associated with that transition [6]. Droop control with the P/ω and Q/V control loops is one of the most commonly used control strategies for the GFCs [6]. However, most of the research of GFCs focused on the inverters which generate sinusoidal voltages by a high-frequency PWM [7]-[13]. There is little research on the grid-forming control of the CMI with an LFM, which has a different control architecture compared with the inverters using a high-frequency PWM with bulky filters.

A fundamental assumption of most classical droop control strategies is that the phase-angle difference between the voltage of the inverter and the voltage of the grid is very small [6], [12], [13]. With this assumption, the Q/V droop control loop can be decoupled from the P/ω control loop and designed independently. However, due to the excellent scalability of the CMI, in MV applications, the CMI would have the capacity to deliver a large amount of active power to the grid. As the consequence, the phase-angle difference between the voltages of the inverter and the grid could be large, resulting in a coupling effect between the P/ω and Q/V control loops. In this circumstance, if there is a large frequency drop in the grid, the active power and the phase-angle difference will be controlled to increase based on the P/ω droop characteristic, but the steady-state reactive power will deviate from its set point due to the increase of the phase-angle difference. Therefore, the reactive power will be affected by the increase of the active power and cannot be controlled independently using the traditional droop control strategies. This is a specific problem with the traditional droop control strategies in the application of CMI with a large active power capacity. However, little research on decoupling the P/ω and Q/V droop control loops in the case of large phase-angle difference has been reported in the literature.
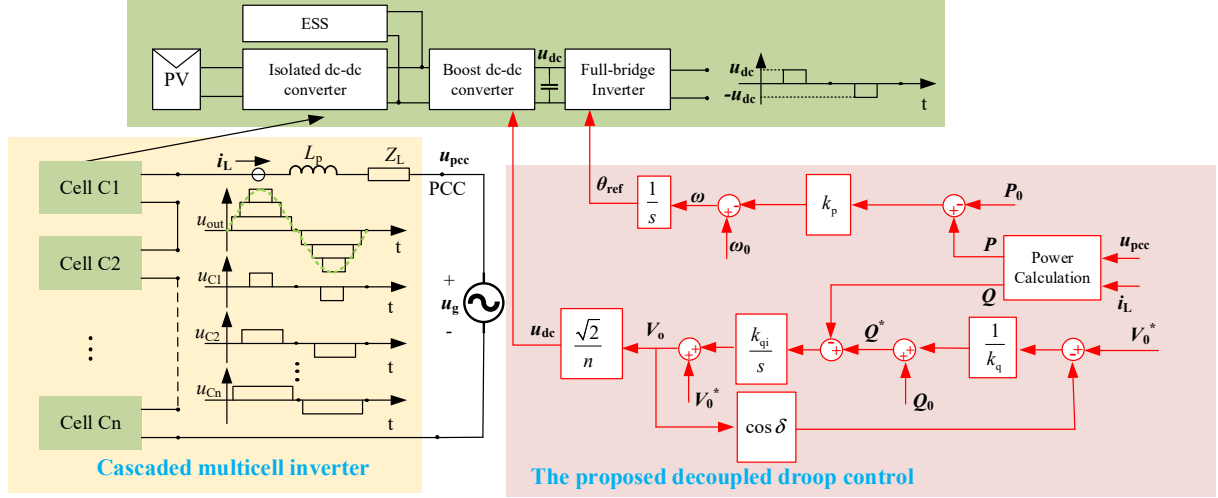
Fig. 1. Schematic of the CMI with the proposed decoupled droop control strategy.
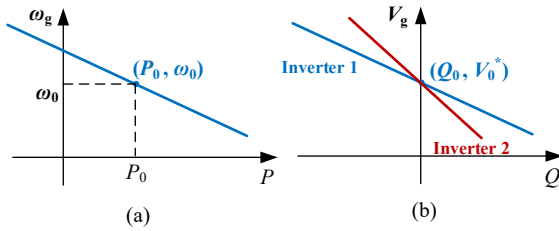

Fig. 2. (a) The P/ω droop characteristic. (b) The Q/V_g droop lines of two inverters with different droop gains k_q.

To address these issues, this paper proposes a decoupled droop control strategy for the CMI with an LFM. A coupling term and an integrator are introduced in the Q/V_g control loop to eliminate the coupling effect from the P/ω control loop. With the proposed strategy, the CMI with an LFM can operate as a GFC to offer an inertia to the grid with an accurate active and reactive power regulation and sharing capability.

II. DECOUPLED DROOP CONTROL FOR CMI USING AN LFM

A. Overall Architecture of the CMI

The overall structure of the CMI with the proposed decoupled droop control strategy is illustrated in Fig. 1. Each cell of the CMI consists of a renewable energy generation device (e.g., a PV array), an isolated dc-dc converter which has an energy storage system (ESS) connected in parallel, a dc-dc boost converter, and a full-bridge inverter. The isolated dc-dc converter can be controlled to enable a maximum power generation from the renewable source. The use of the ESS guarantees a stable power supply for the dc-dc boost converter. The full-bridge inverter uses an LFM and outputs a modified square-wave voltage of the utility frequency. Multiple cells are connected in series to output a staircase voltage waveform which is close to a sinusoidal wave of the utility frequency and meets the THD requirement. The output current is filtered by an optional inductor L_P to meet the current THD requirement of the grid (e.g., < 5%) [14]. It should be noted that the filtering inductor L_P would not be necessary if either a virtual inductive impedance control [6] is introduced or the total line impedance is sufficiently large to filter out the harmonics of the output current to satisfy the current THD requirement [14].

A decoupled droop control strategy, which includes a traditional P/ω droop control loop and a decoupled Q/V_g droop control loop, is proposed for the CMI with an LFM. As shown in Fig. 1, in the proposed Q/V_g droop control loop, a reference value of the reactive power Q^* is firstly generated from a droop-like outer voltage loop; then, the actual reactive power Q is controlled to follow the reference value Q^* through an inner reactive power control loop using an integrator. Moreover, the phase-angle difference δ between the output voltage of the CMI and the grid voltage is introduced in the outer voltage loop, i.e., $\cos \delta$, to eliminate the coupling effect from the active power P/ω droop control loop. The control variable θ_{ref} calculated by the P/ω droop control loop is used for the LFM of the full-bridge inverters, while u_{dc} calculated by the Q/V_g droop control loop is set as the reference output voltage for the dc-dc boost converter in each cell.

B. Proposed Decoupled Droop Control Strategy

Assuming that the total impedance of L_P and line impedance Z_L is nearly purely inductive, the P/ω droop control expressions can be written as:

$$(P - P_0)k_p = -(\omega - \omega_0) \tag{1}$$

$$\delta = \frac{\omega - \omega_g}{s} + \delta_0 \tag{2}$$

$$P = \frac{V_0 V_g}{X} \sin \delta \tag{3}$$

where k_p is the gain of the frequency droop characteristic; (P_0, ω_0) is the fixed set point on the P/ω droop line; V_o and V_g are the root-mean-square (RMS) values of the fundamental components of the CMI output voltage u_{out} and the power grid voltage u_g at the point of common coupling (PCC), respectively; δ is the phase-angle difference between the two voltages and its initial value is δ_0; and X represents the total inductive reactance between the terminal of the CMI and the power grid.

Normally the CMI in the MV application could deliver a large amount of active power to the grid, which makes the phase-angle difference δ vary in a large range. A large variation of δ, caused by the change of the output active power of the CMI, will lead to a large variation of the reactive power due to the term cos δ in the following equation [15], which is commonly used to calculate the reactive power transmission on purely inductive lines.

$$Q = \frac{V_g \left(V_0 \cos \delta - V_g\right)}{X} \tag{4}$$

The phase-angle difference δ in (4) is controlled by the P/ω droop control loop. Due to the coupling term cos δ, the reactive power is indirectly controlled by the P/ω droop control loop, indicating a coupling effect between the P/ω_g and Q/V_g control loops. To eliminate the coupling effect from the P/ω droop control loop, an intuitive solution is to introduce a coupling term cos δ in the Q/V_g droop control loop to make the control of reactive power independent of the variation of δ caused by the P/ω droop control loop. Therefore, in the proposed decoupled Q/V_g droop control, the reference value of the reactive power Q^* is generated by a droop-like outer voltage loop with the coupling term cos δ, and an inner active power control loop is designed to track Q^* using an integrator, as shown in Fig. 1. Then, the reactive power control loop can be expressed as follows.

$$\left(V_0^* - V_0 \cos \delta\right)/k_q = -\left(Q_0 - Q^*\right) \tag{5}$$

$$V_0 = V_0^* + \left(Q^* - Q\right)k_{qi}/s \tag{6}$$

where V_0^* is the rated RMS output voltage of the CMI whose value is set to be the same as the rated RMS grid voltage; k_q is the gain of the Q/V_g droop characteristic; (Q_0, V_0^*) is the fixed set point on the Q/V_g droop line; and Q^* and k_{qi} are the reference reactive power and the gain of the inner integral controller, respectively.

It should be noted that the phase-angle difference δ in (5) can be obtained in several ways. First, according to (3), δ can be approximately obtained by:

$$\delta \approx \sin \delta = \frac{PX}{V_0 V_g} \tag{7}$$

Second, the phase of the grid voltage θ_g can be found by a phase-lock loop. Alternately, a Fourier analysis can be implemented on the grid voltage at the PCC to obtain the phase θ_g of the fundamental component. Then, the phase difference δ is equal to the reference phase θ_{ref} (in the control loop) minus θ_g.

C. Comparison with the Traditional Droop Control

The P/ω droop control used in this paper is the same as the traditional one. The control loop expressed in (1)-(3) is actually a nonuniform oscillator [16], and the steady-state frequency ω of the CMI output voltage would be the same as the grid frequency ω_g despite the change of V_o caused by the Q/V_g control loop if the following condition meets

$$P_0 < \frac{V_0 V_g}{X} \tag{8}$$

Thus, the P/ω droop control can be viewed as a P/ω_g droop control, and the P/ω_g droop curve in Fig. 2(a) follows the characteristic in (1) in the steady state.

On the other hand, the reactive power Q in the steady state with the proposed decoupled Q/V_g droop control can be calculated by (4)-(6) using the final value theorem (FVT) [17]:

$$Q = Q^* = \frac{V_g \left(V_0^* - V_g + k_q Q_0\right)}{k_q V_g + X} \tag{9}$$

There is no coupling term cos δ in (9), and the final value of Q is independent from the P/ω droop control loop. Furthermore, if the value of $k_q V_g$ is much larger than the value of the total line reactance X, the steady state value of Q can be approximately calculated as

$$Q \approx Q_0 + \frac{V_0^* - V_g}{k_q} \tag{10}$$

Therefore, the steady-state reactive power has a clear droop relationship with the variation of the PCC voltage V_g. As shown in Fig. 2(b), if two inverters are connected in parallel to the grid and controlled by the decoupled droop control strategy with the same set point (Q, V_0^*), the reactive power would be shared proportionally between the inverters according to the ratios of their droop gains k_q. When a grid voltage drop occurs at the PCC, the parallelly-connected inverters would deliver reactive power proportionally based on their Q/V_g droop characteristics.

In contrast, the traditional Q/V control can be expressed as

$$\left(V - V_0^*\right)/k_q = -\left(Q - Q_0\right) \tag{11}$$

By combining (4) and (11) and applying the FVT, the steady-state reactive power Q of the inverter using the traditional Q/V droop control is

$$Q = \frac{V_g \left(V_0^* \cos \delta - V_g + k_q Q_0 \cos \delta\right)}{k_q V_g \cos \delta + X} \tag{12}$$

Supposing that the value of $k_q V_g \cos \delta$ is much larger than the value of the total line reactance X, the equation (12) can be simplified as

$$Q \approx Q_0 + \frac{V_0^* \cos \delta - V_g}{k_q \cos \delta} \tag{13}$$

Compared with (12) and (13), there is no coupling term cos δ in (9) and (10), showing that the proposed Q/V reactive power control is independent from the P/ω active power control. Furthermore, the proposed reactive power control has a linear Q/V_g droop characteristic as expressed in (10) if the product of k_q and V_g is much larger than the value of reactance X.

D. The LFM Based on the Area Equivalent Principle

The control variable θ_{ref} is used for the LFM of the full-bridge inverters, while u_{dc} is set as the reference output voltage for the dc-dc boost converters. The LFM is based on the area equivalent principle. Take cell C1 as an example. The inverter of C1 aims to make the top rectangular area with the solid yellow line be equal to the area below the green sinusoidal wave with
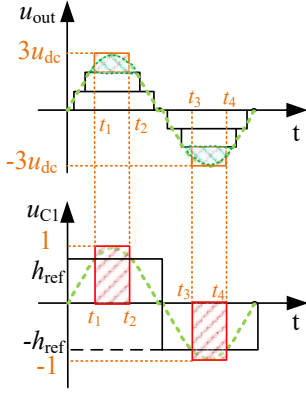
Fig. 3. The LMF strategy of the CMI.

the diamond grid patten, as shown in the top plot of Fig. 3. To this end, $t_1 \sim t_4$ can be easily calculated.

Since the inverter in each cell only regulates the phase of the CMI output voltage u_{out}, another reference signal, which is the dashed-line sine wave with unity amplitude in the bottom plot of Fig. 3, is utilized to compare with the modulation square wave with the amplitude h_{ref}. The value of h_{ref} can be determined by making the reference wave intersect the modulation wave at the times t_1, t_2, t_3, and t_4. As shown in the red shaded area of Fig. 3, when the reference wave is higher than that of the modulation wave during the first half cycle, the inverter of the cell C1 will output a positive pulse. On the contrary, when the reference wave is lower than that of the modulation wave during the second half cycle, the inverter of the cell C1 will output a negative pulse. As a result, the full-bridge inverter of the cell C1 outputs a modified AC square wave at $t_1 \sim t_2$ and $t_3 \sim t_4$ with a magnitude u_{dc}. The amplitude h_{ref} of the modulation square wave of other cells can also be determined by a similar process. Moreover, the control variable θ_{ref} is set as the phase of both the sine reference wave and the modulation square wave of each cell.

III. SIMULATION RESULTS IN A MV APPLICATION

A 2.4 kV, 50 kW, single-phase CMI with 10 cells is set up in MATLAB/Simulink to validate the proposed control strategy. To simplify the simulation, it is assumed that the isolated dc-dc converter, connected in parallel with an ESS, can be controlled to guarantee a sufficient power supply for the dc-dc boost converter, and the dynamics of the DC-link voltage u_{dc}, which is controlled by the dc-dc boost converter, should be much faster than that of the power control loops. Thus, the DC-link voltage of each cell is emulated by using a controlled ideal DC voltage

Table I: Parameters of the CMIs, their Decoupled Droop Control Strategies, and the MV Grid Used in the Simulation Study.

MV Grid						
V_g	2.4 kV	ω_g	120π rad/s	Z_L	$\omega_g L_L$	L_L	15 mH
Control Parameters of CMI 1						
V_0^*	2.4 kV	ω_0	120π rad/s	P_0	100 kW	k_{p1}	**0.0002**
k_{q1}	**0.1**	k_{qi}	0.1414	Q_0	0 Var	L_p	15 mH
Control Parameters of CMI 2						
V_0^*	2.4 kV	ω_0	120π rad/s	P_0	100 kW	k_{p2}	**0.0001**
k_{q2}	**0.05**	k_{qi}	0.1414	Q_0	0 Var	L_p	15 mH

source. The simulation is carried out with two inverters, CMI 1 and CMI 2, which are connected in parallel to the grid. The two inverters share the same parameters except for the droop gains, k_p and k_q. The key parameters are listed in Table I. In the simulation, the phase-angle difference is calculated by the reference phase θ_{ref} (in the control loop) minus the grid voltage phase θ_g obtained from the Fourier analysis on the grid voltage at the PCC.

A. Simulation with a Drop of the Grid Frequency

In the simulation, the initial launch process of the CMIs and their response to a 0.1% drop in the grid frequency from 0.3 s until the end of the simulation are analyzed. As shown in Fig. 4, the output current of the CMI 1 reached a steady state at about 0.15 s after launching; and it took the CMI 1 0.2 s (from 0.3 s to 0.5 s) to stabilize the amplitude of the output current after the drop of the grid frequency. Both the voltage and current meet the THD < 5% requirement in the steady state, and the low-order harmonics take the major portion of their FFT spectra, as shown in Fig. 5. Since CMI 1 and CMI 2 share the same parameters except for the droop gains, the voltage and current waveforms of the CMI 2 are similar to those of the CMI 1. Fig. 6 shows that both CMIs can quickly synchronize their frequency with the grid frequency both in the steady state and after the drop of the grid frequency.

As shown in Fig. 7, the output active power P of both CMIs is stabilized at the set point of 100 kW after the initial launch process. Then, the active power of the CMI 1 followed the designed P/f droop characteristic and increased by 18.3 kW in the steady state after the drop of the grid frequency. Similarly, the steady-state active power of the CMI 2 is increased by 36.6 kW, which is twice the active power increase of the CMI 1 because the ratio of k_{p2} and k_{p1} is 0.5. The phase-angle difference δ of the volage of CMI 1 and the grid voltage is increased from 11.0º to 13.2 º, while the phase-angle difference δ of the volage of CMI 2 and the grid voltage is increased from 11.1º to 15.0º. These values are close to the results calculated using (7). Despite the changes of δ and the active power, the reactive power of both CMIs could always be stabilized at their set point Q_0 of 0 Var, as shown in Fig. 7. The results validate that the reactive power control is decoupled from the P/f control loop.
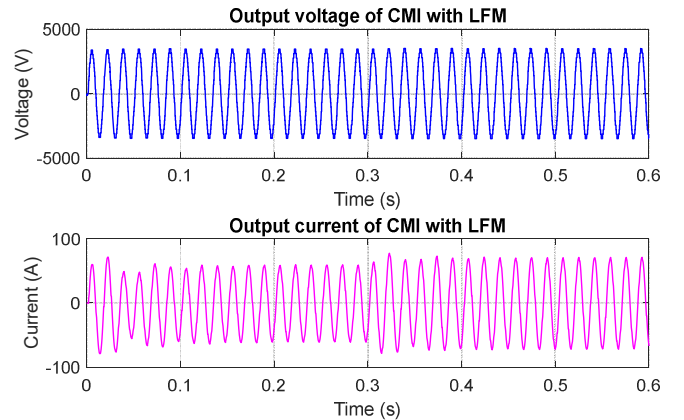

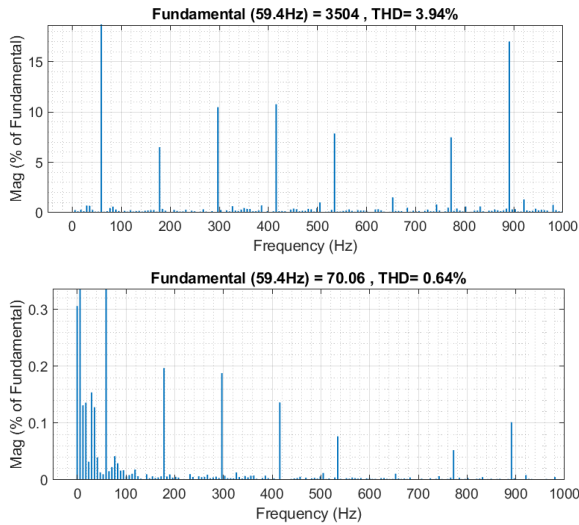Fig. 4. Output voltage and current of the CMI 1 with a 0.1% grid frequency drop.

Fig. 5. FFT analysis of the results of the CMI 1 after 0.5 s: output voltage (top) and output current (bottom).
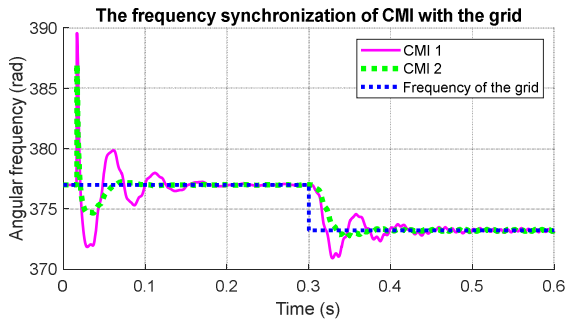

Fig. 6. Frequency synchronization of the CMIs with the grid after the launch process and the 0.1% grid frequency drop.
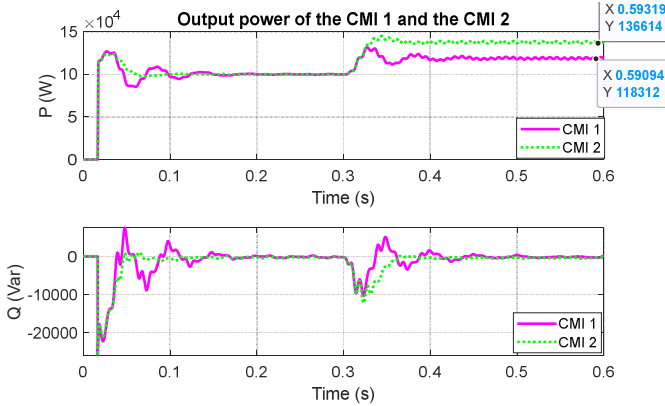

Fig. 7. Active and reactive power outputs of the CMIs with a grid frequency drop.

B. Simulation with a Drop of the Grid Voltage

The RMS value of the grid voltage V_g is set to gradually decrease from 2.4 kV to 2.0 kV within 0.1 s, starting at 0.05 s after the CMIs reached the steady state as discussed in Section III.A. As shown in Fig. 8, after the drop of the grid voltage, the RMS output voltage of the CMI 1 drops from 2460 V to 2116V while the output current increases to offer more reactive power support for the grid. Fig. 9 shows that both the voltage and current meet the THD < 5% requirement in the steady state after

0.35 s. The voltage and current waveforms of CMI 2 are similar to those of the CMI 1 and, thus, are not plotted.

Fig. 10 shows that the angular frequencies of both CMIs could follow the grid frequency and be stabilized at their set point ω_0. As shown in Fig. 11, the output active power P of both CMIs is stabilized at the set point of 100 kW in the steady state, while the reactive power generated by the CMIs in the steady state is proportional to their Q/V_g droop gains. However, there is a small error between the simulated reactive power and the values calculated by (10). For example, the reactive power of CMI 1 is stabilized at about 3600 Var, which is lower than the set point value of 4000 Var obtained from the Q/V_g droop curve expressed by (10). The error between the simulated reactive power and the value obtained from the designed droop curve is caused by the reactance of the line, which is about 5% of the value of $k_{q1}V_g$ and about 10% of the value of $k_{q2}V_g$ for the CMI 1 and CMI 2, respectively. As shown in (9), the error can be reduced by increasing the droop gain of the reactive power control loop (i.e., increasing the power capacity of CMI). When the CMI is connected to a higher-voltage grid, this error could also be reduced. Nevertheless, despite the large phase-angle difference (about 11º for both CMIs), the two CMIs using the proposed decoupled droop control strategy can still output the reactive power proportionally according to the ratio of their reactive power droop control gains.
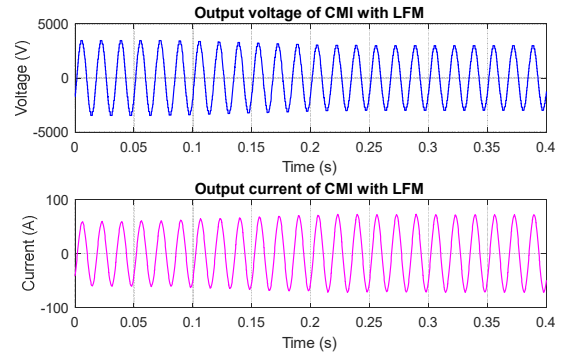

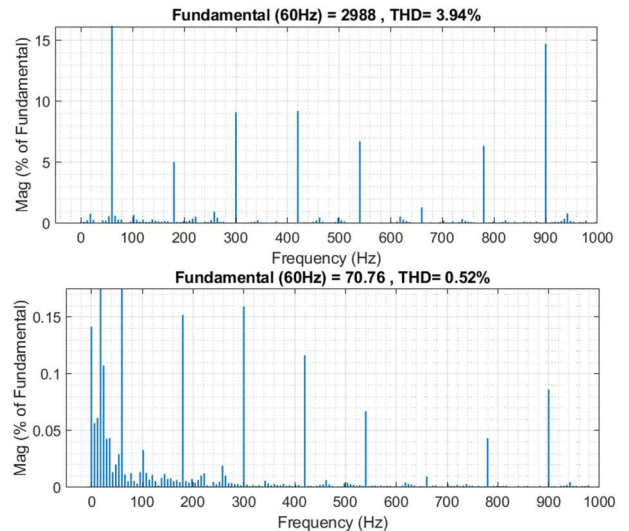Fig. 8. Output voltage and current of the CMI 1 with a grid voltage drop.

Fig. 9. FFT analysis of the results of CMI 1 after 0.35 s: output voltage (top); output current (bottom).
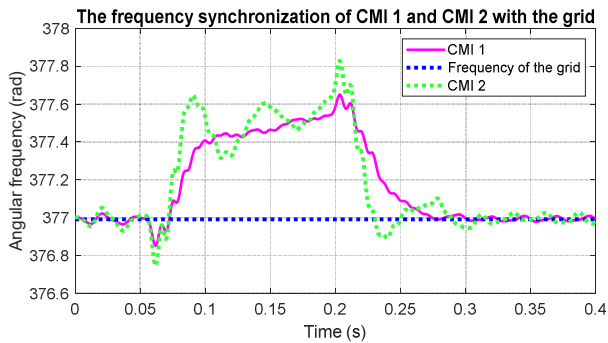
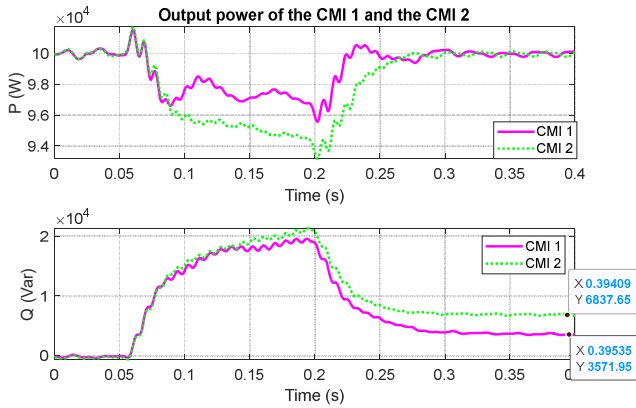Fig. 10. Frequency synchronization of the CMIs with a grid voltage drop.

Fig. 11. Active and reactive power outputs of the CMIs with a grid voltage drop.

IV. CONCLUSIONS AND FUTURE WORKS

This paper proposed a decoupled P/ω_g and Q/V_g droop control strategy for CMIs using LFM. The voltage and phase references generated by the droop control loops were used to control the output voltage of the dc-dc boost converter and the phase of the inverter in each cell, respectively. Simulation results validated that the proposed Q/V_g droop control was successfully decoupled from the P/ω control loop of the CMIs. The simulation results also revealed that parallelly-connected CMIs using the proposed decoupled droop control strategy could share both the active power and reactive power proportionally based on the ratios of their droop control gains.

REFERENCES

[1] J. F. Liu, K. W. E. Cheng, and Y. M. Ye, "A cascaded multilevel inverter based on switched-capacitor for high-frequency AC power distribution System," *IEEE Trans. Power Electron.,* vol. 29, no. 8, pp. 4219-4230, Aug. 2014.

[2] J. Rodriguez, J. S. Lai, and F. Z. Peng, "Multilevel inverters: A survey of topologies, controls, and applications," *IEEE Trans. Ind. Electron.,* vol. 49, no. 4, pp. 724-738, Aug. 2002.

[3] E. Babaei, S. Laali, and Z. Bayat, "A single-phase cascaded multilevel inverter based on a new basic unit with reduced number of power switches," *IEEE Trans. Ind. Electron.,* vol. 62, no. 2, pp. 922-929, Feb. 2015.

[4] H. Zhao, T. Jin, S. Wang, and L. Sun, "A real-time selective harmonic elimination based on a transient-free inner closed-loop control for cascaded multilevel inverters," *IEEE Trans. Power Electron.,* vol. 31, no. 2, pp. 1000-1014, Feb. 2016.

[5] M. Sharifzadeh, H. Vahedi, R. Portillo, L. G. Franquelo, and K. Al-Haddad, "Selective harmonic mitigation based self-elimination of triplen harmonics for single-phase five-level inverters," *IEEE Trans. Power Electron.,* vol. 34, no. 1, pp. 86-96, Jan. 2019.

[6] J. Rocabert, A. Luna, F. Blaabjerg, and P. Rodríguez, "Control of power converters in AC microgrids," *IEEE Trans. Power Electron.,* vol. 27, no. 11, pp. 4734-4749, Nov. 2012.

[7] M. Colombino, D. Gross, J. S. Brouillon, and F. Dorfler, "Global phase and magnitude synchronization of coupled oscillators with application to the control of grid-forming power inverters," *IEEE Trans. Autom. Control,* vol. 64, no. 11, pp. 4496-4511, Nov. 2019.

[8] B. K. Poolla, D. Gross, and F. Dorfler, "Placement and implementation of grid-forming and grid-following virtual inertia and fast frequency response," *IEEE Trans. Power Syst.,* vol. 34, no. 4, pp. 3035-3046, Jul. 2019.

[9] A. Tayyebi, D. Gross, A. Anta, F. Kupzog, and F. Dorfler, "frequency stability of synchronous machines and grid-forming power converters," *IEEE J. Emerg. Sel. Topics Power Electron.,* vol. 8, no. 2, pp. 1004-1018, Jun. 2020.

[10] D. Pan, X. Wang, F. Liu, and R. Shi, "Transient stability of voltage-source converters with grid-forming control: A design-oriented study," *IEEE J. Emerg. Sel. Topics Power Electron.,* vol. 8, no. 2, pp. 1019-1033, Jun. 2020.

[11] R. H. Lasseter, Z. Chen, and D. Pattabiraman, "Grid-forming inverters: A critical asset for the power grid," *IEEE J. Emerg. Sel. Topics Power Electron.,* vol. 8, no. 2, pp. 925-935, Jun. 2020.

[12] T. Wu, Z. Liu, J. Liu, S. Wang, and Z. You, "A unified virtual power decoupling method for droop-controlled parallel inverters in microgrids," *IEEE Trans. Power Electron.,* vol. 31, no. 8, pp. 5587-5603, Aug. 2016.

[13] K. W. Joung, T. Kim, and J.-W. Park, "Decoupled frequency and voltage control for stand-alone microgrid with high renewable penetration," *IEEE Trans. Ind. Appl.,* vol. 55, no. 1, pp. 122-133, Jan.-Feb. 2019.

[14] *IEEE Recommended Practice and Requirements for Harmonic Control in Electric Power Systems (Revision of IEEE Std 519-1992)*, IEEE Standard 519-2014, IEEE Standards Association, Piscataway, NJ, USA, 2014, pp. 1–29.

[15] J. Machowski, Z. Lubosny, J. W. Bialek, and J. R. Bumby, *Power System Dynamics: Stability and Control*, 3rd ed. Hoboken, NJ, USA: Wiley, 2020.

[16] S. H. Strogatz, *Nonlinear Dynamics and Chaos: with Applications to Physics, Biology, Chemistry, and Engineering*, 2nd ed. Boca Raton, FL, USA: CRC press, 2018.

[17] N. S. Nise, *Control Systems Engineering*, 7th ed. Hoboken, NJ, USA: Wiley, 2020.